Spring 2019

Regularized Fourier ptychographic microscopy

Shiqi Xu

Washington University in St. Louis

School of Engineering and Applied Science

Department of Electrical and Systems Engineering

Thesis Examination Committee:
Bruno Sinopoli, Chair
Matthew Lew
Umberto Villa

Regularized Fourier Ptychographic Microscopy

by

Shiqi Xu

A thesis presented to the Graduate School of Engineering
of Washington University in partial fulfillment of the
requirements for the degree of

Master of Science

May 2019
Saint Louis, Missouri

Contents

List of Tables

List of Figures

Acknowledgments

I would gratefully thank professor Ulugbek Kamilov, who agreed to supervise my work and make this thesis possible. The environment in the computational imaging group is phenomenal, and professor Kamilov's door is literally always open. I really appreciate your enthusiasm in teaching and research.

Studying at WashU was such a pleasent experience, surrounded by great professors and students. I was extremely grateful to professor Mattew Lew, who had selflessly supported my work on super-resolution molecular imaging and shared his insights on the fundamental of optics. I would also like to express my deepest appreciation to professor Quing Zhu, who had generously supported my work in biomedical optical imaging. Huge thanks to professor Umberto Villa for his insightful discussions on the photoacoustic image reconstruction. Many thanks to professor Jung-Tsung Shen as well, for the inspirational conversation on advanced optical sensing.

The work was done in collaboration with professor Lei Tian from Boston University, based upon the work supported by the National Science Foundation (NSF) under Grant No. 1813910. I would like to thank to the tremendous contribution professor Tian's group made to this thesis and the generous support from the NSF.

Special thanks to professor Roarke Horstmeyer from Duke University, who was willing to share numerous interesting behind-the-scenes stories on Fourier ptychography and wavefront shaping topics. I also want to thank to professor Gabriel Popescu from University of Illinois, who was the person guided me into the wonderland of optical microscopy.

I would also like to thank my friends and colleagues across the country, too many to name here, whose talent and hardworking gave me the courage to move forward.

Shiqi Xu

Washington University in Saint Louis
May 2019

ABSTRACT OF THE THESIS

Regularized Fourier Ptychographic Microscopy

by

Shiqi Xu

Master of Science in Electrical Engineering

Washington University in St. Louis, May 2019

Research Advisor: Professor Ulugbek Kamilov

Quantitative phase image (QPI) is a popular microscopy technique for studying cell morphology. Recently, Fourier ptychographic microscopy (FPM) has emerged as a low-cost computational microscopy technique for forming high-resolution wide-field QPI images by taking multiple images from different illumination angles. However, the applicability of FPM to dynamic imaging is limited by its high data requirement. In this thesis, we propose new methods for highly compressive FPM imaging using a data-adaptive sparse coding and an online plug-and-play (PnP) method with non-local priors based on the fast iterative shrinkage/threshold algorithm (FISTA). We validate the proposed method on both simulated and experimental data and show that our method is capable of reconstructing images under a significantly lower data rate.

Chapter 1

Introduction

Quantitative phase imaging (QPI) based on optical Fourier ptychographic microscopy (FPM) is a technique for high-resolution, wide field microscopic imaging of semi-transparent cells [10, 18]. In FPM, a programmable LED array is used to illuminate a sample from different angles and create a sequence of low resolution (LR) phaseless images[22]. Reconstruction algorithms are used to computationally combine these LR images into a high resolution (HR) image that overcomes the space-bandwidth product (SBP) limitation[7]. One disadvantage of FPM, comparing with traditional microscopes, is the long data acquisition time due to the need to collect a sequence of images illuminated by multiple LEDs. In the past, sparsely sampled Fourier ptychography has been proposed to improve the frame rate[5]. However, high data-reduction schemes may lead to noise and artifacts in the reconstructed image. Therefore, multiplexed coded illumination has gain popularity, but such method requires improved objective lenses and cameras due to the combination of bright-field and dark-field images[17].

Sparse regularization is a standard approach for enhancing image quality, suppressing noise, and alleviating artifacts. For example, Ren *et al.* [12] developed an FPM algorithm based on edge preserving TV. Alternatively, Zhang *et al.* [21] proposed to use BM3D frames to mitigate Gaussian and Poisson noise. Recently, data-adaptive sparsifying transforms and plug-and-play priors [15, 20] have gained popularity in image reconstruction [11]. These approaches have been shown to improve the quality of image reconstruction by adapting the transform to the statistics of the observed data.

In this thesis, we propose new image reconstruction methods for FPM based on unsupervised dictionary learning and advanced non-local priors. We additionally achieve efficient

processing of the FPM data by using our gradient-based algorithm. We show through simulations and experiments that our method is capable of reconstructing high-quality images from highly under-sampled FPM data.

Chapter 2

Background

In this chapter, we develop important concepts that are related to this thesis. In Section 2.1, we review the propagation of light in free space and reach some principles of Fourier optics. Next, we discuss how to form an optical image using lenses In Section 2.1. We then extend these theories to a microscopy technique called Fourier ptychographic microscopy (FPM). Finally, we introduce a dictionary learning scheme, which will be used to regularize the FPM reconstruction.

2.1 Computing Fourier Transforms with Lenses

In this section, we walk through some classic wave properties of light and how it propagates in free space. An illustration of the setup is shown in fig. 2.1, where a thin lens with a focal distance of f is placed at $z = d$ cm. $f(x, y)$ is the field at $z = 0$ cm. $g(x, y)$ is the field at $z = (d + f)$ cm, which is the back focal plane of the bi-convex thin lens. If we decompose $f(x, y)$ into plane waves, the field $g(x, y)$ can be related to $f(x, y)$ as [14]

$$g(x, y) = h_l \exp\Big[j\pi \frac{(x^2 + y^2)(d - f)}{\lambda f^2}\Big] F\big(\frac{x}{\lambda f}, \frac{y}{\lambda f}\big), \tag{2.1}$$

where

$$h_l = (j/\lambda f) \exp[-jk(d + f)]. \tag{2.2}$$

and $F(\cdot)$ is the Fourier transform of $f(\cdot)$. k is the wavenumber and λ is the wavelength.

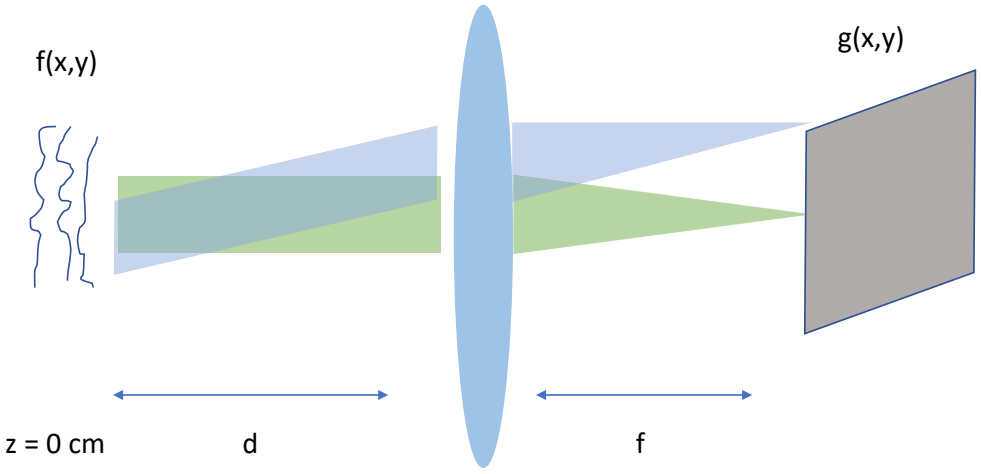

Figure 2.1: An illustration of focusing plane waves in the focal plane. d and f are the distances between $f(x, y)$ and the lens, and the lens and $g(x, y)$, respectively

If we make $d = f$, the exponential term in eq. (2.1) is canceled out, and the relation between $f(x, y)$ and $g(x, y)$ becomes

$$g(x, y) = h_l \, F\big(\frac{x}{\lambda f}, \frac{y}{\lambda f}\big) \propto F\big(\frac{x}{\lambda f}, \frac{y}{\lambda f}\big). \tag{2.3}$$

I.e., the field collected at the back focal plane of a thin lens is proportional to the 2D Fourier transform of the field at the front focal plane of the lens.

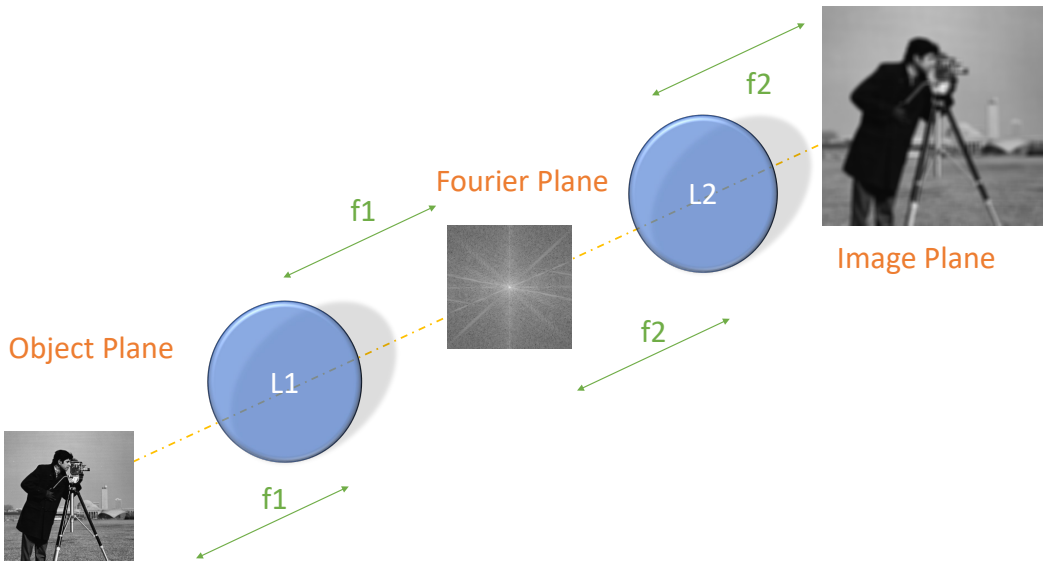

Figure 2.2: An illustration of a imaging system using two lenses, which performs two Fourier transform; so the image is a spatially filtered replica of the object with a magnification

2.2 Image Formation with Two Lenses

We consider a two-lens system illustrated in fig. 2.4, where the imaging object is placed at the front focal plane of the first lens L1, and the image is captured at the back focal plane of the second lens L2. L1 and L2 are separated with (f1+f2). Under Fresnel approximation, the propagation of light can be modeled as two optical Fourier transform of the object, so the image is a spatially filtered replica of the object with a magnification, which can be numerically represented as

$$\mathbf{y} = \mathbf{M}\mathbf{u}, \tag{2.4}$$

where $\mathbf{u} \in \mathbb{R}^P$ is the transparency of the object and the matrix $\mathbf{M} \in \mathbb{C}^{Q\times P}$ denotes the diffraction of the light propagating through lenses.

2.3 Fourier Ptychographic Microscopy

The optical system aforementioned in Section 2.1 is used to create FPM images. The setup does not involve any moving parts, and a low numerical aperture (NA) objective is typically used to provide wider field of view (FOV), longer working distance (WD) and larger depth of field (DOF)[22]. In FPM experiment, a thin slice of two dimensional sample placed at the front focal plane of the convex lens L_1 is illuminated with an approximately monochromatic plane wave created by an LED source, and the intensity of light field at the back focal plane of the lens L_2 is recorded for each illumination, as illustrated in fig.2.3. As introduced in the previous section, the propagation of light through a 2f system can be modeled as a low-passed optical Fourier transform because of the finite NA. FPM utilizes both normal and oblique illuminations to bypass the frequency limit. Owing to the shift theorem of the Fourier transform, the modulation of a thin sample by a plane wave with wavevector (k_x,k_y) is equivalent to shifting the frequency components of the sample by (k_x,k_y). Therefore, the high frequencies can still be preserved after the low-pass filtering. Numerically, the forward model can be expressed as

$$\mathbf{b} = \mathcal{H}(\mathbf{x}) =\mid \mathbf{Mu}(\mathbf{x}) \mid^2, \tag{2.5}$$

where $\mathbf{x} \in \mathbb{R}^P$ is the phase of the object. The vector $\mathbf{u}(\mathbf{x}) = \exp(i\mathbf{x})$ accounts for the transmission of the imaging object. The matrix $\mathbf{M} \in \mathbb{C}^{Q\times P}$ denotes the diffraction of the light propagating through lenses; it is implemented by taking the discrete Fourier transform (DFT) of the object, shifting the frequency spectrum, truncating the low frequency region, multiplying it by a pupil function in the frequency domain, and taking the inverse DFT. Finally, the intensity of optical field is recorded with a photonic device.

2.4 Data Adaptive Sparse Representation

Patch-wised dictionary learning has been widely used as a data-adaptive image reconstruction. Assuming that the image $\mathbf{x} \in \mathbb{R}^P$ can be approximated as a linear combination of

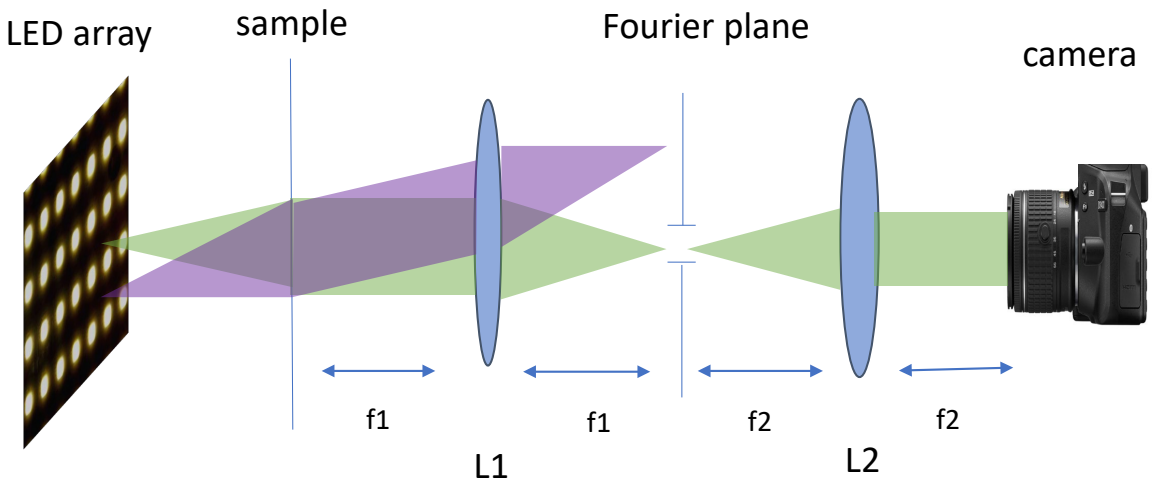

Figure 2.3: An illustration of a FPM imaging system, where an led array is used as illumination sources.

learned basis vectors, we divide the image into small overlapping patches $\mathbf{y}_j \in \mathbb{R}^K$and synthesize each patch with columns of a dictionary $\mathbf{D} \in \mathbb{R}^{K\times M}$

$$\mathbf{y}_j \approx \mathbf{D}\mathbf{a}_j \tag{2.6}$$

where $\mathbf{a}_j \in \mathbb{R}^M$ is sparse, i.e,$\|\mathbf{a}_j\|_0 \ll K$[6,8]. Thus, for an image $\mathbf{x}$, consisting of n different patches $\{\mathbf{y}_1, ..., \mathbf{y}_N\}$, we could formulate the following dictionary learning scheme

$$\min_{\mathbf{D},\mathbf{a}_j} \sum_{j=1}^{N} \frac{1}{2}\|\mathbf{D}\mathbf{a}_j - \mathbf{y}_j\|_2^2 + \lambda \sum_{j=1}^{N} \|\mathbf{a}_j\|_1 \quad s.t. \quad \mathbf{D} \in \mathcal{C} \tag{2.7}$$

where $\mathbf{a}_1, ..\mathbf{a}_N$ are the decomposition coefficients of the signals, and each column of $\mathbf{D} = (\mathbf{d}_1, ..., \mathbf{d}_M)$ is a basis atom. The ℓ_1-term in (2.7) promotes sparsity in the coefficients $\mathbf{a}_j$, and $\lambda > 0$ is the weight for this penalty. In (2.7), the set

$$\mathcal{C} \triangleq \{\mathbf{D} : \|\mathbf{d}_j\|_2 = 1 \quad \forall j\}, \tag{2.8}$$

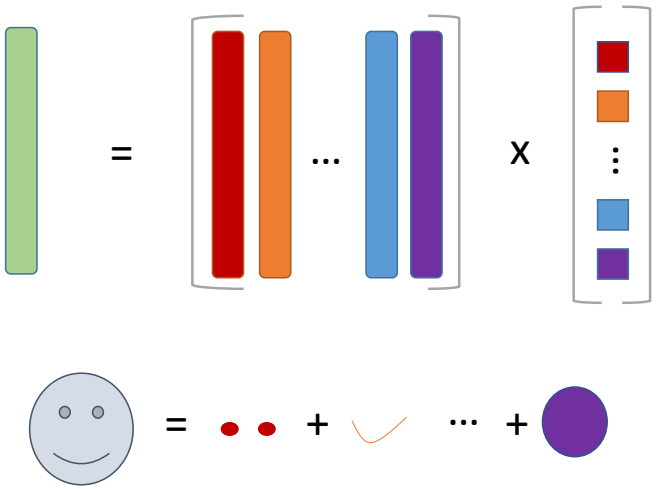

Figure 2.4: An illustration of how atoms in a dictionary are used to approximate an image

is used to constrain the atoms in the dictionary to avoid scaling ambiguities[9]. Accordingly, we can rewrite (2.7) as the following optimization problem

$$\min_{\mathbf{D},\mathbf{A}} \frac{1}{2}\|\mathbf{DA} - \mathcal{P}(\mathbf{x})|_{\mathrm{F}}^2 + \lambda\|\mathbf{A}\|_1, \tag{2.9}$$

where $\mathcal{P}(\cdot)$ represents a patch-extraction operation and the matrix $\mathbf{A} = (\mathbf{a}_1, ..., \mathbf{a}_N)$. Notice that the objective function is nonconvex jointly. Hence, the optimization for this unsupervised learning formulation is usually done alternatively for $\mathbf{A}$ and $\mathbf{D}$.

Chapter 3

Dictionary Learning Regularized FPM

3.1 Problem formulation

The image reconstruction problem can be formulated as the following joint optimization problem

$$\{\widehat{\mathbf{x}}, \widehat{\mathbf{D}}, \widehat{\mathbf{A}}\} = \underset{\mathbf{x},\mathbf{D},\mathbf{A}}{\operatorname{argmin}} \mathcal{L}(\mathbf{x}, \mathbf{D}, \mathbf{A}) \tag{3.1}$$

$$\begin{aligned}\mathcal{L}(\mathbf{x}, \mathbf{D}, \mathbf{A}) := \frac{1}{2}\|\mathbf{b} - \mathcal{H}(\mathbf{x})\|_2^2 + \frac{\gamma}{2}\|\mathbf{DA} - \mathcal{P}(\mathbf{x})\|_{\mathrm{F}}^2 \\ + \lambda\|\mathbf{A}\|_1 + \tau\mathcal{R}(\mathbf{x}),\end{aligned} \tag{3.2}$$

where $\mathbf{x} \in \mathbb{R}^P$, $\mathbf{D} \in \mathcal{C}$, and $\mathbf{A} \in \mathbb{R}^{M\times N}$ are imaging object, dictionary, and sparse coding coefficients from Section 2.4. $\mathcal{H}(\cdot)$ is the forward operator modeling light propagation, as discussed in Section 2.3, and $\mathcal{P}(\cdot)$ is the patch extraction operator extracting patches from the object image $\mathbf{x}$. The first quadratic term in (3.2) measures the fidelity with respect to the physical model. The second quadratic term measures the accuraty of the image approximation by a linear combination of dictionary atoms, while the ℓ_1-term promotes the sparsity of coding coefficients. The forth term is another regularizer such as isotropic TV [13]. We next discuss how individual problem is solved. Algorithm 1 summarizes the steps for solving this joint optimization problem.

Algorithm 1 Sparsely coded FPM reconstruction

input: $\hat{\mathbf{x}}^0$, $\mathbf{D}^0 \in \{\text{DCT}\}$, L measurements $\mathbf{b}_l$ where $l \in 1, ...L$, step size β, regularization parameters γ, λ, τ.
set: $\mathbf{s}_0 \leftarrow \hat{\mathbf{x}}^0$, $q_0 \leftarrow 1$
for $t = 1, 2, \ldots$ **do**
  $\mathbf{z}^t \leftarrow \mathbf{s}^{t-1} - (\beta/L) \sum_{l=1}^{L} \nabla \mathcal{D}_l(\mathbf{x})$ ▷ eq.(3.5)
  $\hat{\mathbf{x}}^t \leftarrow \text{prox}_{\mathcal{R}}(\mathbf{z}^t, \beta\tau)$
  $q_t \leftarrow \frac{1}{2}\left(1 + \sqrt{1 + 4q_{t-1}^2}\right)$
  $\mathbf{s}^t \leftarrow \hat{\mathbf{x}}^t + ((q_{t-1} - 1)/q_t)(\hat{\mathbf{x}}^t - \hat{\mathbf{x}}^{t-1})$
  for $k = 1, 2, \ldots$ **do**
    $\mathbf{A}^k \leftarrow \text{updateA}(\mathbf{A}^{k-1}, \mathbf{D}^{k-1}, \mathbf{s}^t, \gamma, \lambda)$ ▷ eq.(3.9)
    $\mathbf{D}^k \leftarrow \text{updateD}(\mathbf{A}^k, \mathbf{D}^{k-1}, \mathbf{s}^t, \gamma, \lambda)$ ▷ eq.(3.14)
  end for
end for

3.2 Image Reconstruction

Define $\mathcal{Y}$ as the operator that stitches small image patches to form the whole image. We can re-write the $\mathbf{x}$ optimization problem as

$$\widehat{\mathbf{x}} = \underset{\mathbf{x}}{\text{argmin}}\, \mathcal{L}(\mathbf{x}, \mathbf{D}, \mathbf{A}) = \underset{\mathbf{x}}{\text{argmin}}\, \{\mathcal{D}(\mathbf{x}) + \tau\mathcal{R}(\mathbf{x})\} \tag{3.3}$$

where

$$\mathcal{D}(\mathbf{x}) = \frac{1}{2}\|\mathbf{b} - \mathcal{H}(\mathbf{x})\|_2^2 + \frac{\gamma}{2}\|\mathcal{Y}(\mathbf{DA}) - \mathbf{x}\|_2^2 \tag{3.4}$$

and $\mathcal{R}(\cdot)$ is the isotropic TV operator[13]. $\tau > 0$ controls the strength of the regularization. Problem (3.3) is solved using accelerated proximal gradient method[1]. The gradient expression is given by:

$$\begin{aligned}\frac{\partial}{\partial \mathbf{x}}\mathcal{D}(\mathbf{x}) = [\frac{\partial}{\partial \mathbf{x}}\Psi(\mathbf{x})]^H \text{diag}(\Psi(\mathbf{x}))(\mathcal{H}(\mathbf{x}) - \mathbf{b}) \\ +\gamma(\mathbf{x} - \mathcal{Y}(\mathbf{DA}))\end{aligned} \tag{3.5}$$

where

$$\Psi(\mathbf{x}) = \mathbf{M}\mathbf{u}(\mathbf{x}), \quad [\frac{\partial}{\partial \mathbf{x}}\Psi(\mathbf{x})]^H = \text{diag}(\overline{i\exp(i\mathbf{x})})\mathbf{M}^H. \tag{3.6}$$

$[\cdot]^H$ is the adjoint operator. The proximal operator of $\mathcal{R}(x)$ is implemented in the dual-domain as discussed in [1].

3.3 Sparse Coding

We consider the problem

$$\widehat{\mathbf{A}} = \underset{\mathbf{A}}{\operatorname{argmin}} \mathcal{L}(\mathbf{x}, \mathbf{D}, \mathbf{A}) \tag{3.7a}$$

$$= \underset{\mathbf{A}}{\operatorname{argmin}} \left\{ \frac{1}{2} \|\mathbf{DA} - \mathcal{P}(\mathbf{x})\|_{\mathrm{F}}^2 + \lambda_a \|\mathbf{A}\|_1 \right\} \tag{3.7b}$$

where $\lambda_a = \frac{\lambda}{\gamma}$. This optimization can be solved using alternating direction method of multipliers (ADMM). Rewriting (3.7b) as a suitable form for ADMM, we introduce auxiliary variable $\mathbf{B} \in \mathbb{R}^{M \times N}$ and have

$$\underset{\mathbf{A},\mathbf{B}}{\operatorname{argmin}} \left\{ \frac{1}{2} \|\mathbf{DA} - \mathcal{P}(\mathbf{x})\|_{\mathrm{F}}^2 + \lambda_a \|\mathbf{B}\|_1 \right\} \quad \text{s.t.} \quad \mathbf{A} - \mathbf{B} = \mathbf{0}, \tag{3.8}$$

which can be solved through following iterations with dual variable $\mathbf{U} \in \mathbb{R}^{M \times N}$[2]:

$$\mathbf{A}^{k+1} = \underset{\mathbf{A}}{\operatorname{argmin}} \left\{ \frac{1}{2} \|\mathbf{DA} - \mathcal{P}(\mathbf{x})\|_{\mathrm{F}}^2 + \frac{\rho}{2} \|\mathbf{A} - \mathbf{B}^k + \mathbf{U}^k\|_{\mathrm{F}}^2 \right\} \tag{3.9a}$$

$$\mathbf{B}^{k+1} = \underset{\mathbf{B}}{\operatorname{argmin}} \left\{ \lambda_a \|\mathbf{B}\|_1 + \frac{\rho}{2} \|\mathbf{A}^{k+1} - \mathbf{B} + \mathbf{U}^k\|_{\mathrm{F}}^2 \right\} \tag{3.9b}$$

$$\mathbf{U}^{k+1} = \mathbf{U}^k + \mathbf{A}^{k+1} - \mathbf{B}^{k+1}. \tag{3.9c}$$

The sub-problem (3.9b) is solved with shrinkage operation as

$$\mathbf{B}^{k+1} = \mathcal{S}_{\lambda/\rho}(\mathbf{A}^k + \mathbf{U}^k) \tag{3.10}$$

where

$$\mathcal{S}_\eta(\mathbf{X}) = \operatorname{sign}(\mathbf{X}) \odot \max(0, \mid \mathbf{X} \mid -\eta). \tag{3.11}$$

The sub-problem (3.9a) can be efficiently solved with following iterations[3]:

$$\{\mathbf{D}_L, \mathbf{D}_U\} = \mathcal{LU}(\mathbf{D}\mathbf{D}^H) \tag{3.12a}$$

$$\mathbf{A} = \mathcal{P}(\mathbf{x})\mathbf{D}_U^{-1}\mathbf{D}_L^{-1} \tag{3.12b}$$

where $\mathcal{LU}$ is the lower-upper(LU) matrix decomposition. $\mathbf{D}_L, \mathbf{D}_U$ are the permuted lower triangular matrix and upper triangular matrix factorized from $\mathbf{D}$, respectively.

3.4 Dictionary Update

The dictionary update step can be formulated as solving

$$\widehat{\mathbf{D}} = \underset{\mathbf{D}}{\operatorname{argmin}}\, \mathcal{L}(\mathbf{x}, \mathbf{D}, \mathbf{A}) \tag{3.13a}$$

$$\text{s.t.} \quad \|\mathbf{d}_i\|_2^2 = 1 \quad \text{for} \quad i \in \{1, 2, 3..M\}, \tag{3.13b}$$

which can be solved in a similar way as sub-problem (3.9a), plus a projection step.

$$\{\mathbf{A}_L, \mathbf{A}_U\} = \mathcal{LU}(\mathbf{A}\mathbf{A}^H) \tag{3.14a}$$

$$\mathbf{D} = \mathcal{P}(\mathbf{x})\mathbf{A}_U^{-1}\mathbf{A}_L^{-1} \tag{3.14b}$$

$$\mathbf{d}_i = \frac{\mathbf{d}_i}{\|\mathbf{d}_i\|_2^2} \quad i \in \{1, 2, 3..M\}, \tag{3.14c}$$

where $\mathbf{A}_L, \mathbf{A}_U$ are the permuted lower triangular matrix and upper triangular matrix factorized from $\mathbf{A}$, respectively.

3.5 Numerical Experiments

The data acquisition setup used here for both simulated and experimental measurement has been discussed in [18]. A 32×32 surface-mounted LED array with 4 mm pitch is placed 70 mm above the sample, and 513 nm light with 20 nm bandwidth is used for illumination. The NA of the objective is 0.2, whilst the achieved synthetic NA is around 0.70, as the sum of objective

NA and illumination NA, when central 293 LEDs are used. We conduct and compare reconstructions with Newton's method using Tikhonov regularization[18] and gradient-based method using no regularization, TV regularization, and proposed regularization. During the sparse coding step, the image is cropped into 16×16 small patches with sliding step-size of one pixel. The 256 dictionary atoms are initialized with first 256 DCT bases.

3.5.1 Simulated Data

We simulate the measurements on 10 images chosen from the USC-SIPI Image Database[19] using the forward model discussed in (2.5) using $12, 16$, and 24 LEDs. The images are resized to 1000×1000. The LED positions are carefully selected to yield approximately equivalent SBP, which is a key evaluation of the throughput of an optical imaging system[7, 22]. Gaussian noise with standard deviation $\sigma = 0.05 \times \max(\mathbf{b})$ is added to the measurement. Figure 3.1 exemplifies the reconstructed image of *Lenna* from 16 measurements. The reconstructed image with no regularization is severely contaminated by the granular speckle noise. Although TV regularization successfully suppresses this noise, some high-frequency details are also lost due to the piece-wise constant assumption. Table 3.1 lists the signal to noise ratio of reconstruction results from simulation using 12, 16, and 24 LEDs. As expected, on average the proposed method gives highest SNR images than other regularization approaches. The hyper-parameters for each method are selected such that the method gives the highest SNR.

3.5.2 Experimental Data

We further evaluate the proposed method on human cells. Figure 3.2 and Figure 3.3 examplify the resconstructed images of human cervical adenocarcinoma epithelial (HeLa) cells and human osteosarcoma epithelia(U2OS) cells. Reconstructions using 293 measurements with Newton's method discussed in [17] are presented as reference. In reconstructed HeLa images using 16 measurements with no regularization, we can clearly see grating artifacts as reported in[5]. Despite that TV regularization is able to reduce the noise in the image, it results in blocky artifacts. A similar situation is observed for reconstructions of U2OS cells. Additionally, we have tested the method in [17] using 16 measurements; however, the

Table 3.1: SNR values for reconstructed images from different number of measurements in dB

	12 meas.			**16 meas.**			**24 meas.**		
Image	NoReg	TV	Proposed	NoReg	TV	Proposed	NoReg	TV	Proposed
Lenna	10.74	15.05	15.61	11.06	12.89	16.02	11.68	14.51	16.34
Elaine	10.36	15.51	15.80	10.33	15.75	16.94	11.14	15.81	16.44
Cameraman	12.70	16.60	18.14	12.42	17.77	19.70	12.63	16.96	18.18
Barbara	7.01	7.67	9.06	7.16	7.76	9.10	7.53	9.14	9.54
House	9.82	11.95	13.19	9.78	12.45	13.78	10.91	13.22	13.81
Male	10.04	11.33	12.82	10.28	11.55	13.38	10.81	11.55	13.31
Boat	9.92	12.41	13.97	9.94	13.04	14.23	10.61	13.02	14.42
Peppers	11.66	14.67	17.05	11.80	15.25	18.00	12.49	14.67	18.58
Westconcord	10.71	11.88	13.79	10.73	12.15	14.00	11.75	13.72	14.63
Clock	12.47	17.06	17.54	12.63	17.32	16.31	12.80	17.48	18.83
Average	10.54	13.41	14.70	10.61	13.69	15.23	11.24	14.01	15.41

method failed to reconstruct meaningful images so we ommitted the corresponding results from the figure.

Figure 3.1: Comparison of reconstruction results for *Lenna* from 16 measurements. (a) shows the original images. (b), (c), and (d) present results using no regularization (NoReg), TV regularization (TV) and proposed regularization (Proposed), respectively. Each image is labeled with its SNR value with respect to the original image.

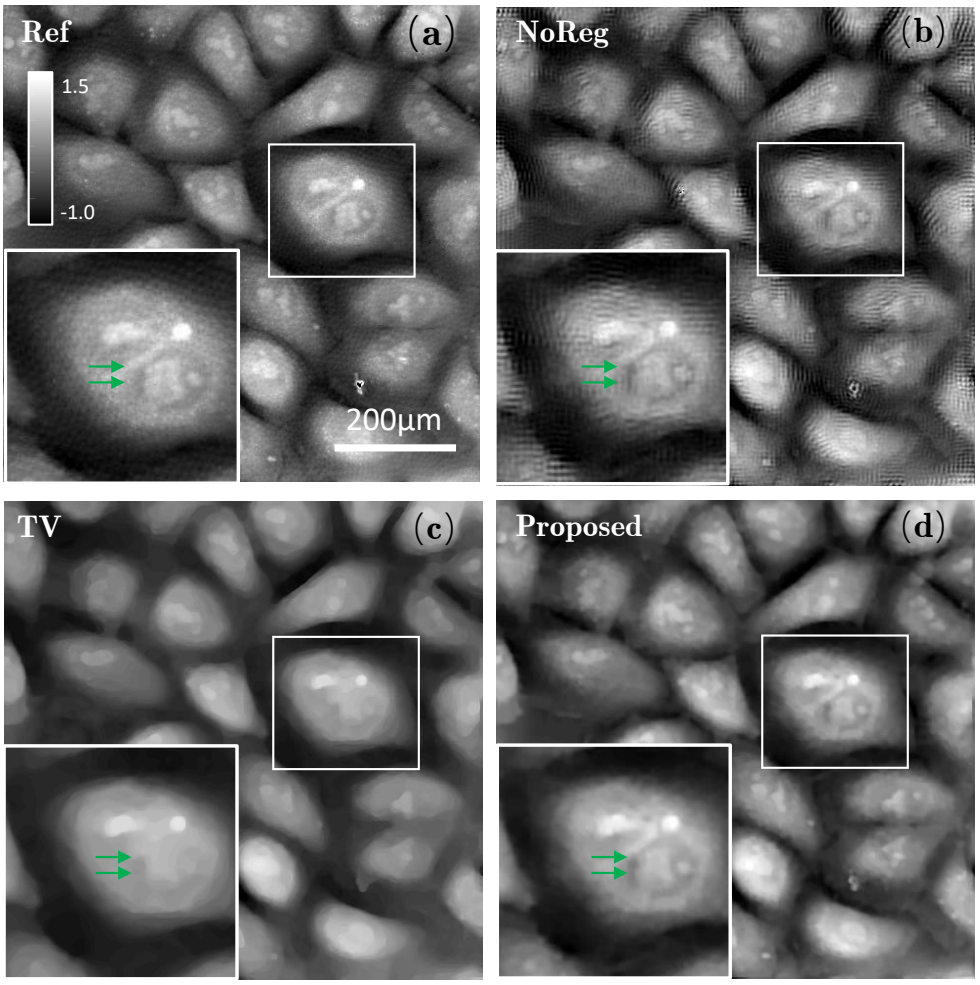

Figure 3.2: Comparison of four algorithms on experimental HeLa dataset. (a) shows the reconstruction with 293 measurements using the Newton's method with Tikhonov regularizaiton[17]. (b), (c) and (d) present results using 16 measurements with no regularization, TV regularization and proposed regularization, respectively.

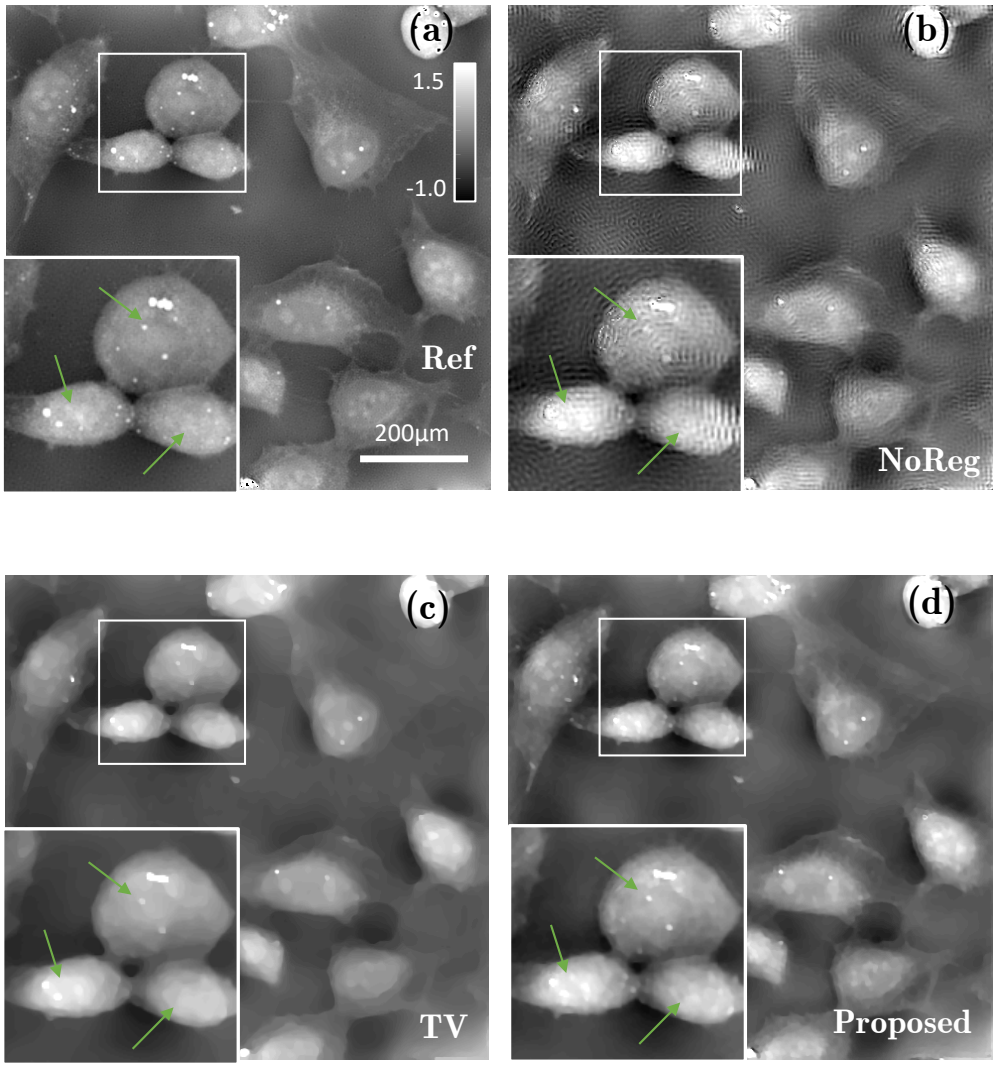

Figure 3.3: Comparison of reconstruction results for U2OS cells. (a) shows the reconstruction with 293 measurements using Newton's method with Tikhonov regularizaiton[17]. (b), (c) and (d) present results with 16 LEDs using NoReg, TV, and Proposed, respectively.

Chapter 4

Advanced Priors Beyond Optimization

4.1 Denoiser as a Prior

The idea, origianlly proposed by Venkatakrishnan *et. al.*, was to regularize the image reconstruction by denoising[20]. Rather than compute the proximal operator of a written cost function, we use a more general denoising operator $\mathsf{denoise}_\sigma(\cdot)$ to remove artifacts from the image, termed plugin-and-play priors (PnP) for reconstruction[15, 16].

An theoretical convergence of PnP-ISTA was given in the recent paper by Yu *et.al.* [15], which argues that PnP-ISTA converges to a fixed point at the rate of O(1/t) if $\mathsf{denoise}_\sigma(\cdot)$ is a θ-averaged operator. Here, we shift the online PnP-ISTA to online PnP-FISTA (PnP-FISTA-Online) for better convergence rate, and discuss its advantages over the PnP-FISTA using full gradient(PnP-FISTA-Full).

Algorithm 2 PnP-SGD

input: $\mathbf{x}^0 = \mathbf{s}^0$, $\gamma > 0$, $\sigma > 0$, $\{q_k\}_{k\in\mathbb{N}}$, and $B \geq 1$
for $k = 1, 2, \ldots$ **do**
    $\mathbf{z}^k \leftarrow \mathbf{s}^{k-1} - \gamma\hat{\nabla} d(\mathbf{s}^{k-1})$
    $\mathbf{x}^k \leftarrow \mathsf{denoise}_\sigma(\boldsymbol{z}^k)$
    $\mathbf{s}^k \leftarrow \mathbf{x}^k + ((q_{k-1} - 1)/q_k)(\boldsymbol{x}^k - \mathbf{x}^{k-1})$
end for

4.2 Proposed Method

In this section, we introduce our PnP-FISTA-Online for Fourier ptychographic micrsocopy (FPM) reconstruction. In FPM, the data-fidelity term d

$$d(\mathbf{x}) = \mathbb{E}[d_j(\mathbf{x})] = \frac{1}{J}\sum_{j=1}^{J} d_j(\mathbf{x}), \tag{4.1}$$

contains a large number of component functions, where each d_j only depends on a subset of the measurements$\mathbf{y}$. The gradient of $d(\mathbf{x})$ is calculated from the expected value of the gradient of each measurement

$$\nabla d(\mathbf{x}) = \mathbb{E}[\nabla d_j(\mathbf{x})] = \frac{1}{J}\sum_{j=1}^{J} \nabla d_j(\mathbf{x}). \tag{4.2}$$

The key idea of our method, summarized in Algorithm 2, is to approximate the gradient at each iteration with the expectation of B components from its subset

$$\hat{\nabla} d(\mathbf{x}) = \frac{1}{B}\sum_{b=1}^{B} \nabla d_{j_b}(\mathbf{x}), \tag{4.3}$$

with $B \ll J$. Moreover, $j_1, \ldots, j_B$ are independent random variables that are distributed uniformly over $\{1, \ldots, J\}$.

4.3 Numerical Validation

In this section, we present results on both simulated and experimental data. We consider two representative denoisers: a edge-preserving isotropic TV[13] operator and a non-local BM3D[4] denoiser.

4.3.1 Simulated Data

We quantitatively analyze the performance of the proposed method by reconstructing six gray-scale images (*Cameraman, House, Jet, Lenna, Pepper* and *Woman*) chosen from the USC-SIPI Image Database[19] using the forward model discussed in (2.5). The measurements were corrupted by an additive Gaussian noise (AWGN) corresponding to 40 dB of input SNR.

Figure 4.1 shows the visual reconstruction results of the *cameraman* image, labeled with the average SNRs obtained from the reconstruction results from six images using different algorithm. We observe that the advanced non-local plugin prior (BM3D) gives superior results than the edge-preserving TV. Figure 4.2 demonstrates the reconstructed image SNR evolution with respect to time. We conclude that the BM3D-online method converges near to the BM3D-full method at a much faster speed with respect to time.

4.3.2 Real Data

We use the same experimental setup and samples discussed in Section 3.5. Reconstruction results of the human cervical adenocarcinoma epithelial (HeLa) cells are presented in fig.4.3. Each image has the resolution of 1000×1000 pixels. We use a batch size of $B = 60$ measurements. We see that under no regularization, some unnatural features are presented, such as the horizontal streaking artifacts. Both TV and BM3D mitigate this artifact , but the TV method generate blockiness in the cell, while online-BM3D algorithms improve the visual quality in general.

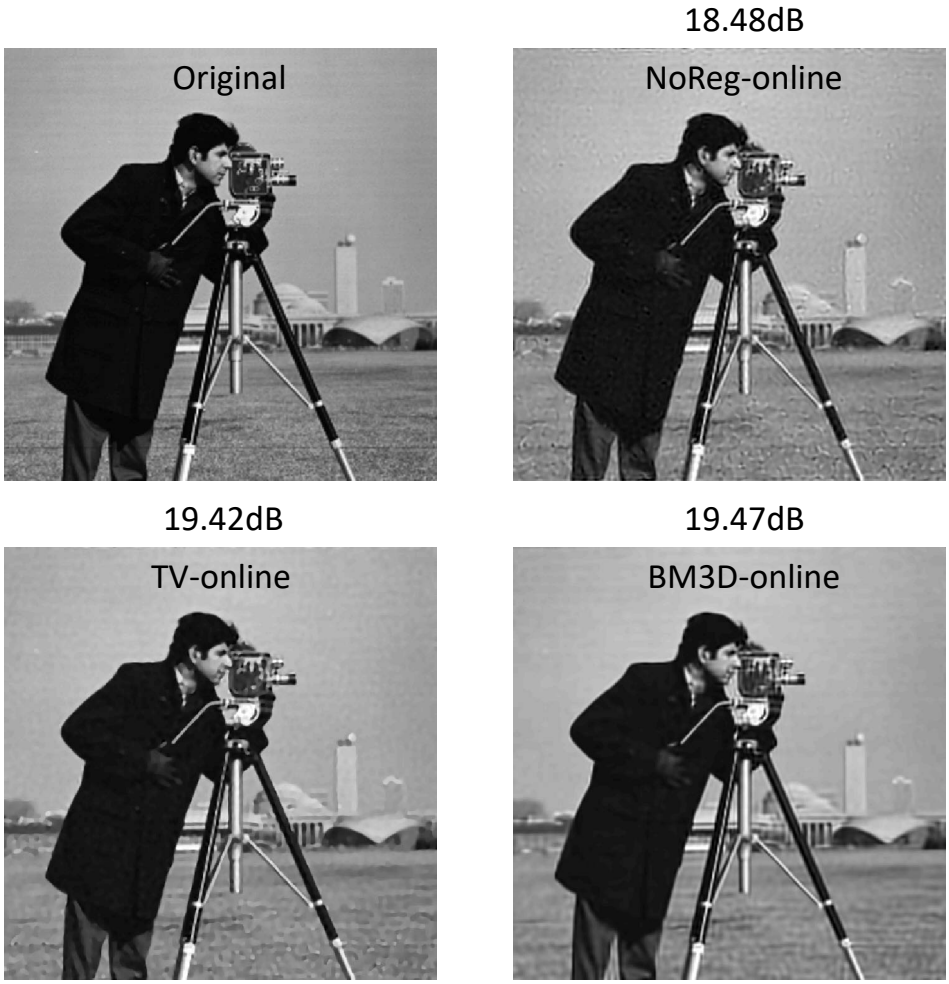

Figure 4.1: Comparison of reconstruction results for *Cameraman* using batch size $B = 60$. (a) shows the original images. (b), (c), and (d) present results using no regularization (NoReg), TV regularization (TV) and PnP-BM3D (BM3D) regularization, respectively. Each image is labeled with the average SNR value from six images for the algorithm used with respect to the original image.

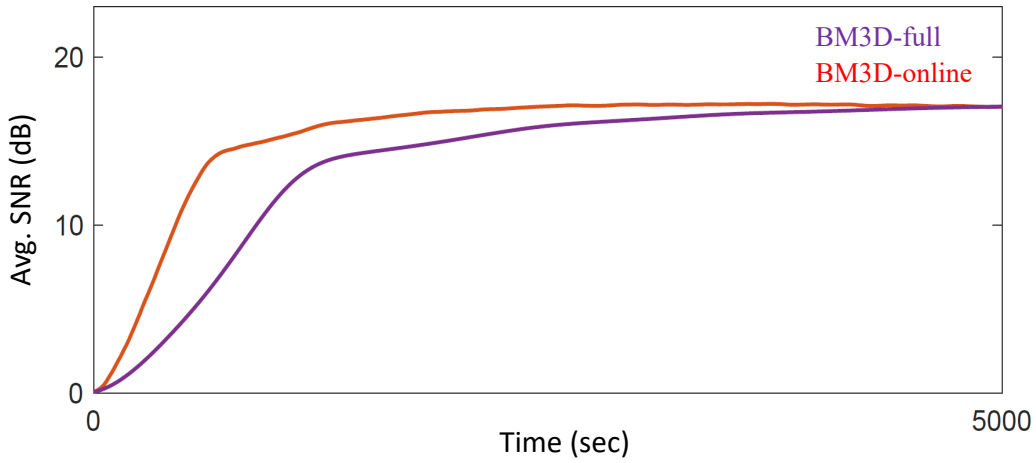

Figure 4.2: Comparison of reconstruction time between BM3D-full and BM3D-online. The BM3D-online uses a batch size $B = 60$. The BM3D-full use all 293 measurements.

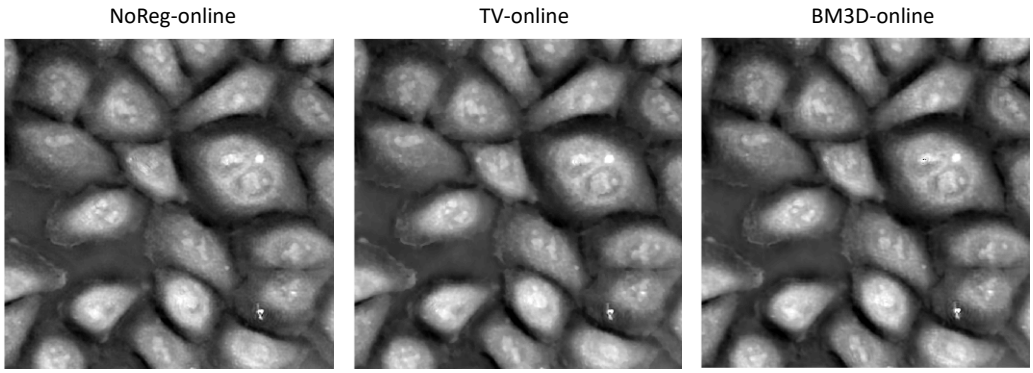

Figure 4.3: Comparison of reconstruction results for HeLa cells using batch size $B = 60$. (a), (b), and (c) present results using no regularization (NoReg), TV regularization (TV) and PnP-BM3D (BM3D) regularization, respectively.

Chapter 5

Conclusion

To conclude, in this thesis, we propose novel dictionary learning and online plug-and-play algorithm for the regularized FPM reconstruction. Numerical experiments demonstrate that our methods are able to reconstruct high quality phase of the unstained cells quantitatively with highly under-sampled data. We show that unsupervised dictionary learning and PnP-BM3D are able to remove the artifacts while preserve the details of an image. Moreover, we demonstrates that our online PnP algorithm converges to a near-optimal point faster in time than the full gradient one. The work can be extended to other convex and non-convex inverse problems with advanced plugin priors.

References

[1] Amir Beck and Marc Teboulle. Fast gradient-based algorithms for constrained total variation image denoising and deblurring problems. *IEEE Transactions on Image Processing*, 18(11):2419–2434, 2009.

[2] Stephen Boyd, Neal Parikh, Eric Chu, Borja Peleato, Jonathan Eckstein, et al. Distributed optimization and statistical learning via the alternating direction method of multipliers. *Foundations and Trends® in Machine learning*, 3(1):1–122, 2011.

[3] Scott Shaobing Chen, David L Donoho, and Michael A Saunders. Atomic decomposition by basis pursuit. *SIAM review*, 43(1):129–159, 2001.

[4] Aram Danielyan, Vladimir Katkovnik, and Karen Egiazarian. Bm3d frames and variational image deblurring. *IEEE Transactions on Image Processing*, 21(4):1715–1728, 2012.

[5] Siyuan Dong, Zichao Bian, Radhika Shiradkar, and Guoan Zheng. Sparsely sampled fourier ptychography. *Optics express*, 22(5):5455–5464, 2014.

[6] Michael Elad and Michal Aharon. Image denoising via sparse and redundant representations over learned dictionaries. *IEEE Transactions on Image processing*, 15(12):3736–3745, 2006.

[7] Adolf W Lohmann, Rainer G Dorsch, David Mendlovic, Zeev Zalevsky, and Carlos Ferreira. Space–bandwidth product of optical signals and systems. *JOSA A*, 13(3):470–473, 1996.

[8] Julien Mairal, Francis Bach, Jean Ponce, and Guillermo Sapiro. Online dictionary learning for sparse coding. In *Proceedings of the 26th annual international conference on machine learning*, pages 689–696. ACM, 2009.

[9] Bruno A Olshausen and David J Field. Emergence of simple-cell receptive field properties by learning a sparse code for natural images. *Nature*, 381(6583):607, 1996.

[10] Xiaoze Ou, Roarke Horstmeyer, Changhuei Yang, and Guoan Zheng. Quantitative phase imaging via fourier ptychographic microscopy. *Optics letters*, 38(22):4845–4848, 2013.

[11] Saiprasad Ravishankar and Yoram Bresler. Mr image reconstruction from highly undersampled k-space data by dictionary learning. *IEEE transactions on medical imaging*, 30(5):1028–1041, 2011.

[12] David Ren, Emrah Bostan, Li-Hao Yeh, and Laura Waller. Total-variation regularized fourier ptychographic microscopy with multiplexed coded illumination. In *Mathematics in Imaging*, pages MM3C–5. Optical Society of America, 2017.

[13] Leonid I Rudin, Stanley Osher, and Emad Fatemi. Nonlinear total variation based noise removal algorithms. *Physica D: nonlinear phenomena*, 60(1-4):259–268, 1992.

[14] Bahaa EA Saleh and Malvin Carl Teich. *Fundamentals of photonics*. John Wiley & Sons, 2019.

[15] Yu Sun, Brendt Wohlberg, and Ulugbek S Kamilov. An online plug-and-play algorithm for regularized image reconstruction. *IEEE Transactions on Computational Imaging*, 2019.

[16] Yu Sun, Shiqi Xu, Yunzhe Li, Lei Tian, Brendt Wohlberg, and Ulugbek S Kamilov. Regularized fourier ptychography using an online plug-and-play algorithm. *arXiv preprint arXiv:1811.00120*, 2018.

[17] Lei Tian, Xiao Li, Kannan Ramchandran, and Laura Waller. Multiplexed coded illumination for fourier ptychography with an led array microscope. *Biomedical optics express*, 5(7):2376–2389, 2014.

[18] Lei Tian, Ziji Liu, Li-Hao Yeh, Michael Chen, Jingshan Zhong, and Laura Waller. Computational illumination for high-speed in vitro fourier ptychographic microscopy. *Optica*, 2(10):904–911, 2015.

[19] USC. The usc-sipi image database, images available http://sipi.usc.edu/database/.

[20] Singanallur V Venkatakrishnan, Charles A Bouman, and Brendt Wohlberg. Plug-and-play priors for model based reconstruction. In *2013 IEEE Global Conference on Signal and Information Processing*, pages 945–948. IEEE, 2013.

[21] Yongbing Zhang, Pengming Song, Jian Zhang, and Qionghai Dai. Fourier ptychographic microscopy with sparse representation. *Scientific Reports*, 7(1):8664, 2017.

[22] Guoan Zheng, Roarke Horstmeyer, and Changhuei Yang. Wide-field, high-resolution fourier ptychographic microscopy. *Nature photonics*, 7(9):739, 2013.

Vita

Shiqi Xu

Degrees

B.S. in Electrical Engineering, UIUC, December 2016

M.S. in Electrical Engineering (expected), WUSTL, May 2019

In Press Publication

Xu, S. Uddin, S. Zhu, Q. (2019). "Improving DOT reconstruction with Born iterative method and US-guided sparse regularization." *Biomedical optics express* **10**(5).

Yu, S. Xu, S. Li, Y. Tian, L. Wohlberg, B. Kamilov, U. (2019). "Regularized Fourier ptychography using an Online Plug-and-Play Algorithm.", *Proc. IEEE Int. Conf. Acoustics, Speech and Signal Process*, 2019.

Honors and Awards

2016	UIUC ECE Senior Project DSP Area Award
2019-2021	Duke BME Scholar Award

May 2019